

Photo-driven bacterial motor for tumor-targeted deep penetration and destruction while reducing hepatotoxicity

Meng Zhang^a, Huifang Nie^a, Guangwei Jiang^a, Cyrille Boyer^c, Dan Peer^d,
Rongqin Huang^{a,b,*} 

^a School of Pharmacy, Key Laboratory of Smart Drug Delivery (Ministry of Education), National Key Laboratory of Advanced Drug Formulations for Overcoming Delivery Barriers, Fudan University, Shanghai 201203, China

^b Academy of Medical Sciences, Tianjian Laboratory of Advanced Biomedical Sciences, The Third Affiliated Hospital, Zhengzhou University, Zhengzhou 450001, China

^c Australian Centre for Nanomedicine, School of Chemical Engineering, University of New South Wales, Sydney, NSW 2052, Australia

^d Laboratory of Precision Nanomedicine, The Shmunis School of Biomedicine and Cancer Research, George S. Wise Faculty of Life Sciences, Tel Aviv University, Tel Aviv-Yafo 6997801, Israel

ARTICLE INFO

Keywords:

Bacterial motor
Photothermal driving
Tumor deep penetration
Targeting therapy

ABSTRACT

Live bacteria-based therapeutics show immense promise in cancer treatment due to their combined tumor-killing and immune-modulating functions. However, their clinical application is limited by their vulnerability to macrophage clearance, their struggle to penetrate deeply into tumors due to their micron-scale size, and their high off-target liver toxicity. In this study, we present the concept of "targeted photothermal microbial motor". This motor is created by loading photothermal nanoparticles onto the clinical attenuated *Salmonella typhimurium* VNP20009 (VNP) and encapsulating them within a macrophage membrane (IP@VNP@M). The encapsulation within the M1 macrophage membrane provides the motor with tumor-targeting enrichment capacity. Notably, this tumor-enriched bacterial motor can stimulate accelerated bacterial movement (a 4.0-fold increase in speed) under mild photothermal excitation by near-infrared (NIR) light. This acceleration, combined with the bacteria's hypoxia-targeting ability, enables deep tumor penetration and high uptake. The photothermal bacterial motor utilizes the synergy of photothermal effects and bacteria to polarize M2 phenotypic tumor-associated macrophages into the M1 phenotype. This results in efficient tumor killing and triggers a robust anti-tumor immune response, significantly extending the survival of tumor-bearing mice. Importantly, this precise tumor-targeting capability of the bacterial motor allows them to avoid the hepatotoxicity typically induced by VNP. Therefore, the bacterial motor presents a promising alternative for bacteria-based tumor therapy, offering enhanced efficacy and reduced toxicity.

Introduction

Tumors significantly threaten human health and well-being[1,2]. The primary clinical strategies for tumor management include surgery, radiotherapy and chemotherapy[3–5]. However, the potential for incomplete surgical removal and the low specificity of radiotherapy and chemotherapy often result in tumor recurrence and severe toxic side effects. The burgeoning field of immunotherapy has shown great potential, primarily due to its capacity to prevent the spread and return of cancerous cells[6,7]. Yet, the immunosuppressive microenvironment of solid tumors and high interstitial pressures frequently lead to inadequate

immune activation and ineffective tumor immune responses. Consequently, there is a critical need to explore new therapies that effectively eliminate tumors, activate anti-tumor immunity, and minimize toxic side effects.

Recent discoveries have shown that natural bacterial infections can exert an antitumor effect on malignant tumors, drawing significant attention to the use of live bacteria in cancer treatment[8]. Researchers have utilized attenuated *Mycobacterium tuberculosis* to develop Bacillus Calmette-Guerin (BCG) vaccines, leveraging the immunomodulatory properties of bacteria[9]. This method has proven effective in treating aggressive localized bladder cancer for decades. Bacterial therapy, as an

* Corresponding author at: School of Pharmacy, Key Laboratory of Smart Drug Delivery (Ministry of Education), National Key Laboratory of Advanced Drug Formulations for Overcoming Delivery Barriers, Fudan University, Shanghai 201203, China.

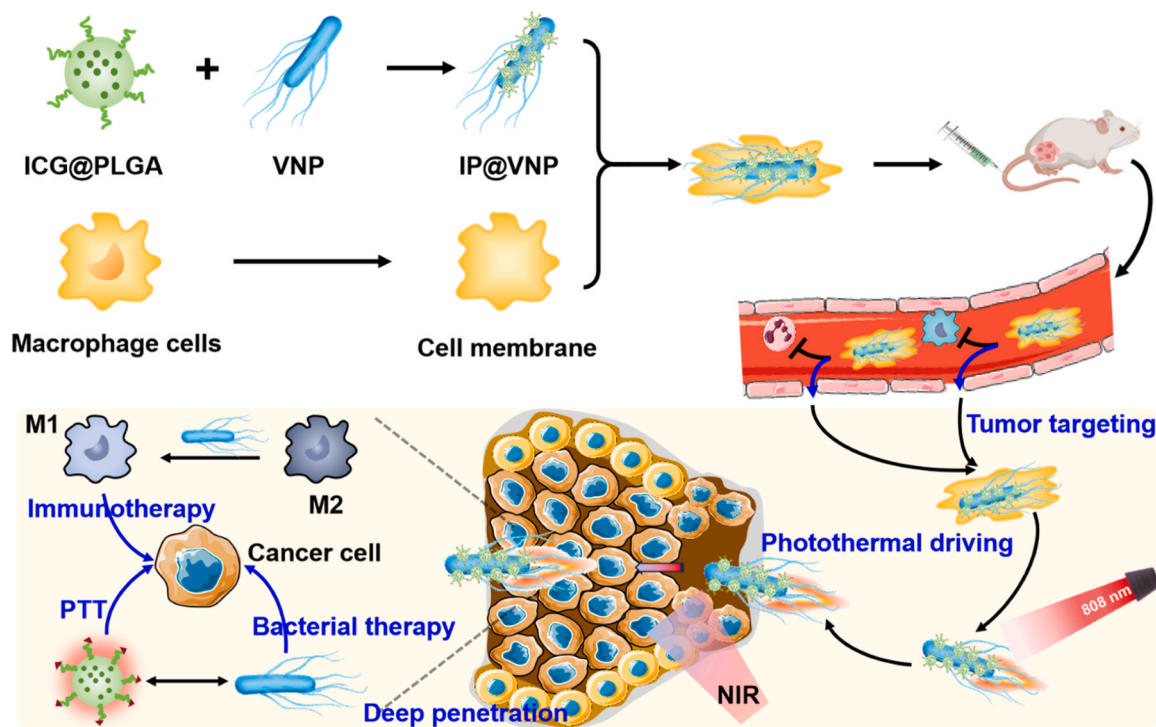
E-mail address: rqhuang@fudan.edu.cn (R. Huang).

<https://doi.org/10.1016/j.nantod.2025.102752>

Received 13 November 2024; Received in revised form 26 February 2025; Accepted 31 March 2025

Available online 10 April 2025

1748-0132/© 2025 Elsevier Ltd. All rights are reserved, including those for text and data mining, AI training, and similar technologies.



Scheme 1. a) Schematic illustration of the fabrication of IP@VNP@M. b) A scheme illustrating the process of tumor targeting, tumor penetration and combined therapy.

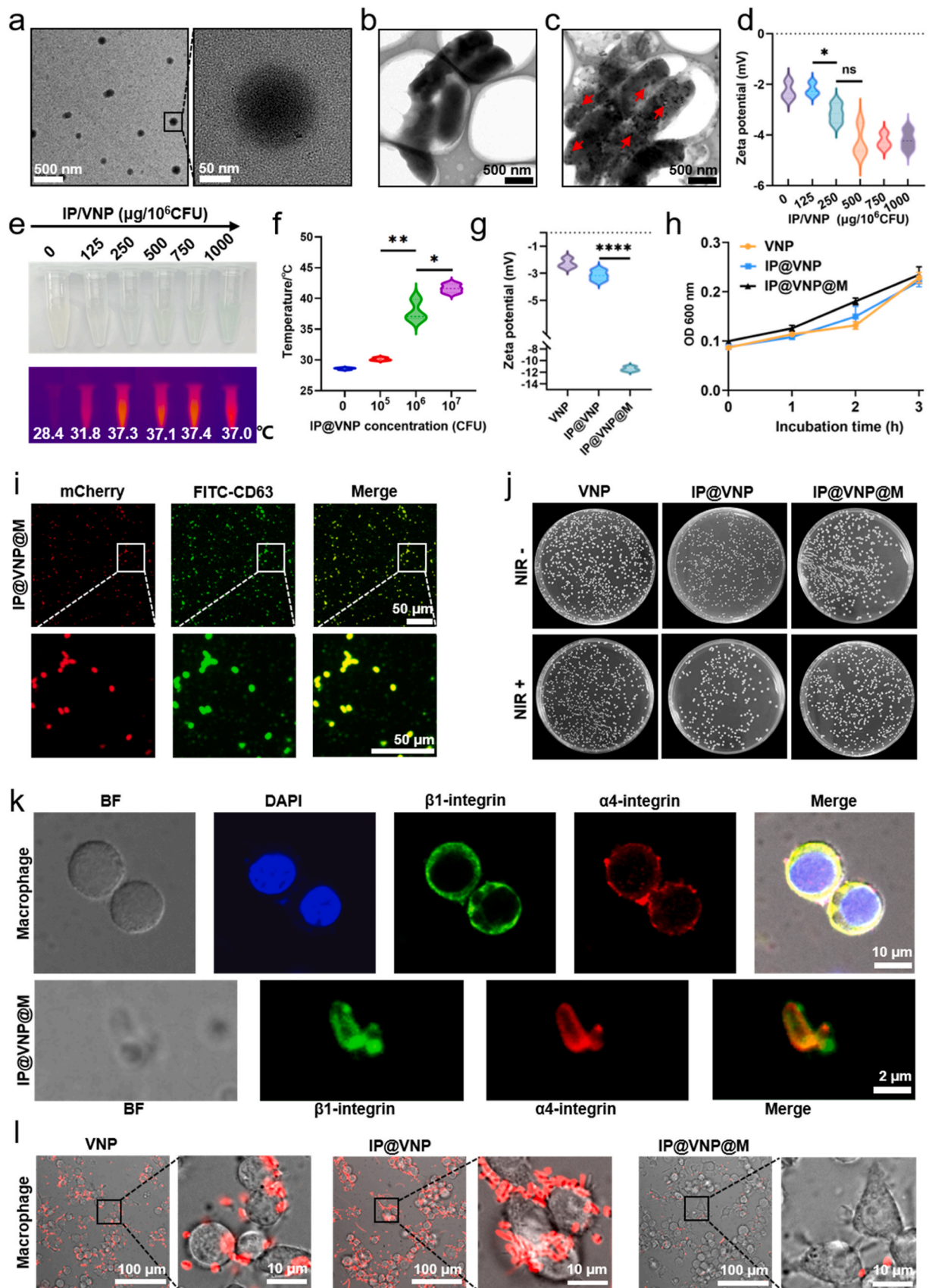
emerging method for treating tumors, mainly works through direct oncolysis, immune induction, interference with tumor cell metabolism, and disruption of tumor blood vessels and microenvironments. Typically, microbial communities tend to colonize tumors preferentially, thriving in the hypoxic conditions and unique metabolite profiles present within tumors, creating an ideal environment for anaerobic bacteria [10]. Importantly, bacteria can reprogram immune cells, shifting them from an immunosuppressive to an immune-activated state, thus bolstering anti-tumor immunity [11,12]. *Salmonella typhimurium* VNP20009 (VNP), an engineered strain, has been designed for enhanced tumor targeting and reduced toxicity, appropriate for the initial phase I clinical investigation in participants suffering from disseminated melanoma and kidney cell carcinoma [13]. Despite some success, the therapeutic outcomes of using live bacteria have been limited by inadequate drug efficacy and significant toxicity. The large size of bacteria and the high interstitial fluid pressure within tumors hinder bacterial penetration, while their exogenous nature makes them susceptible to capture by macrophages or accumulation in non-tumor tissues, leading to severe toxic side effects and reduced treatment efficiency [14,15]. For example, Gram-negative bacteria can release endotoxins upon destruction, triggering a strong immune response [16]. This can lead to a cytokine storm, causing extensive tissue damage, disrupting physiological functions, and potentially resulting in severe organ pathology or even death if not managed promptly. Therefore, enhancing the deep penetration of tumors, improving the tumor targeting ability of bacteria and reducing the side effects are imperative for improving bacterial cancer therapy [17, 18].

Micromotors are micro structures, exhibiting self-propelled motion and the ability to coordinate actions, emulate the functionalities of biological entities by transforming various forms of energy into kinetic activity. Bacteria, as living organisms, are inherently motile due to the presence of flagella on their surface. The flagellum, the motile organ of bacteria, is a unique protein nanomotor [19]. At low temperatures, bacteria enter a physiological state known as "dormancy" [20]. As the temperature gradually increases to the bacteria's optimal growth range, they "wake up" and resume their normal physiological activities. For

certain motile bacteria with flagella, an increase in temperature enhances their motility. Enhanced bacterial motility can improve their deep penetration into tumor sites. To further advance the clinical translational application, the bacterium was loaded with the clinically approved near-infrared fluorophore (indocyanine green (ICG)) (IP@VNP). The mild photothermal effects under near-infrared (NIR) could accelerate bacterial movement.

To further protect the transport of bacteria in venous blood, coating with the macrophage membrane could significantly improve targeting and delivery to metastatic sites [21,22]. In this context, polarizing macrophages towards an anti-tumor phenotype through drug stimulation offers a promising cancer treatment approach. Given that M0 macrophages are in a non-polarized initial state characterized by relatively low expression levels of immune-related molecules on the cell membrane, this condition diminishes the probability of recognition and clearance by the immune system. Consequently, the drug-delivery system can circulate more stably and effectively exert its therapeutic effects. Combining this strategy with controllable photothermal therapy, which uses photothermal energy to enhance bacterial penetration and tumor eradication, presents a novel cancer therapy strategy.

Therefore, this study introduces photothermal bacteria cloaked in macrophage membranes, outfitted with a photothermal drive for targeting and destroying deep tumor tissues. These camouflaged bacteria reduce bacterial clearance in the bloodstream, facilitating remote drug delivery and deep tumor penetration through NIR photothermal action. Injected via the tail vein, the camouflaged bacteria accumulate in tumors, alleviate systemic inflammation, and protect the liver from bacterial damage. On 4T1 triple-negative breast cancer, these disguised bacteria achieve deep tumor penetration, induce inflammatory factors, and polarize tumor-associated macrophages (TAM) into M1 subtypes, offering a novel tumor treatment strategy by transforming the tumor immune microenvironment and combining the photothermal therapy (Scheme 1).



(caption on next page)

Fig. 1. Construction and performance evaluation of IP@VNP@M. a) TEM image and enlarged image of IP. b) TEM image of VNP. c) TEM representation of IP@VNP. d) The zeta potential of VNP after loading with different concentrations of IP. e) The image of VNP after loading with different concentrations of IP and photothermal profile of IP@VNP aqueous solution under NIR light exposure for a duration of 5 min. f) The temperature changes with different concentrations of IP@VNP. g) Zeta potential of VNP, IP@VNP and IP@VNP@M. h) Growth curves of VNP, IP@VNP and IP@VNP@M, maintained in Luria-Bertani broth at 37 °C, with optical density at 600 nm recorded at specified intervals. i) LSCM images of IP@VNP@M. FITC-CD63 was used to localize the macrophage membrane, and mCherry was auto-fluorescence of VNP. j) The colony distribution of VNP, IP@VNP and IP@VNP@M after NIR light exposure (1.0 W cm⁻², 5 min). k) LSCM images of macrophages, and IP@VNP@M, with green highlighting cell membranes stained with FITC-conjugated anti-CD49d antibody (α 4-integrin), red indicating cell membranes stained with PE-conjugated anti-CD29 antibody (β 1-integrin), and blue representing nuclei stained with DAPI. l) The uptake of VNP, IP@VNP and IP@VNP@M in macrophage. Data are presented as mean \pm SD (n = 3). Statistical significance was calculated by one-way ANOVA using the Tukey post-test, giving *P* values. * *P* < 0.05, ** *P* < 0.01, **** *P* < 0.0001. ns denotes non-significant.

Results

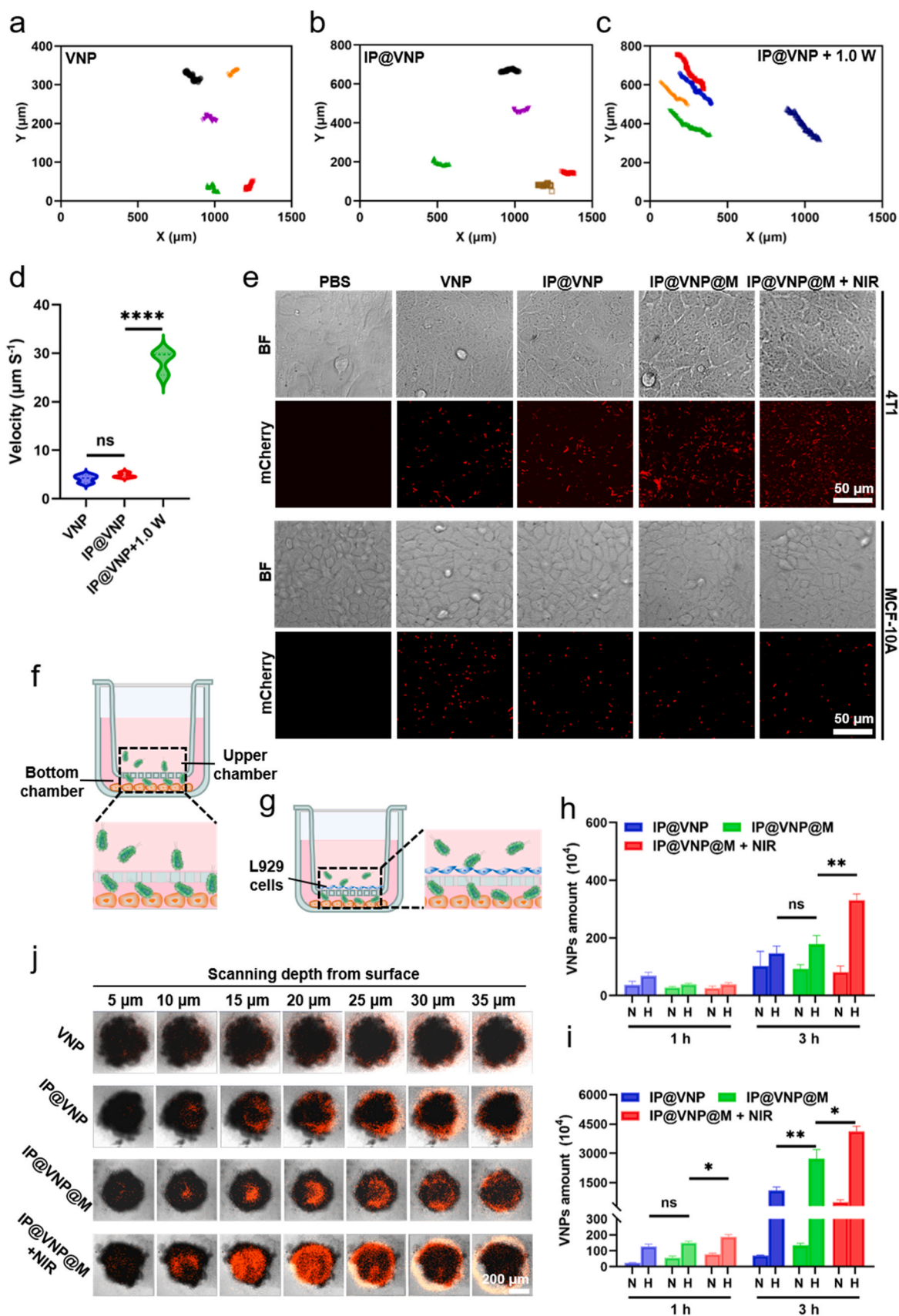
To prepare the macrophage membrane-cloaked photothermal bacteria, photothermal nanoparticles comprising PLGA-encapsulated ICG (IP nanoparticles) were initially synthesized using the double emulsion water-in-oil-in-water (W/O/W) method, as depicted in Fig. 1a and S1. The resulting images showed that the nanoparticles were uniformly dispersed and possessed a symmetrical structure with an average diameter of around 115 nm (Fig. 1a), and a larger size for Dynamic light scattering (DLS) (Figure S2). The IP nanoparticles exhibited excellent dispersibility and a surface charge of -29.9 mV (Figure S3), along with notable NIR photothermal properties (Figure S4). The drug loading capacity for ICG was optimized at 55.67 %, enhancing the photothermal effect for subsequent bacterial integration. TEM images revealed a smooth bacterial surface free from nanoparticles (Fig. 1b), whereas bacteria harboring the nanoparticles exhibited a clear particle distribution on their surface (Fig. 1c). Due to the presence of carboxyl groups on the PLGA surface (Figure S3, S5), the IP nanoparticles were functionalized and anchored to the surface of VNP bacteria via the interaction between the carboxyl and amino groups, which led to a decrease in the bacteria's surface charge (Fig. 1d). Consequently, the maximum loading of IP on bacteria reached $250 \mu\text{g IP}/10^6 \text{ CFU}$ (Fig. 1d, e), with the IP nanoparticles uniformly distributed across the bacterial surface. Compared to untreated bacteria, the IP-loaded bacteria (IP@VNP) exhibited enhanced NIR heating capabilities. However, due to the optimized ICG loading, the photothermal effect of IP@VNP remained moderate. When subjected to 808 nm light for 5 min, IP@VNP at a concentration of $250 \mu\text{g mL}^{-1}$ achieved a temperature increase up to 37.3 °C (Fig. 1e). Based on these results, a concentration of 10^6 CFU/mL for IP@VNP was selected for final administration (Fig. 1f). Subsequently, the macrophage membrane was applied to the surface of IP@VNP using the membrane extrusion technique. The macrophage membrane was marked with red fluorescent m-Cherry for bacterial labeling and green fluorescent FITC-CD63. Laser Scanning Confocal Microscopy (LSCM) observation confirmed a complete and uniform coverage of the macrophage membrane on IP@VNP, as indicated by the complete overlap of green and red signals (Fig. 1i). By contrast, the pure VNP and IP@VNP group displayed no green fluorescence (Figure S6). To further confirm successful membrane encapsulation, LSCM was used to examine macrophage cells for the expression of α 4 and β 1 integrins (Fig. 1k). Analysis of the encapsulated bacteria's surface also demonstrated fluorescent signals for α 4 and β 1 integrins, verifying the successful extraction of macrophage membranes and their effective incorporation onto the bacterial surface (Fig. 1k). Additionally, due to the negative charge of the cell membrane, the surface charge of IP@VNP@M decreased to -11.4 mV, a reduction from the charge observed in IP@VNP (Fig. 1g). Importantly, the modifications involving IP nanoparticles and cell membrane encapsulation did not significantly impair bacterial viability. This was evidenced by the gradual increase in optical density (OD_{600 nm}) over time (Fig. 1h). Particularly noteworthy is that, despite the mild photothermal effect achieved by optimizing photothermal nanoparticle loading, both IP@VNP and IP@VNP@M retained high bacterial viability even after exposure to 808 nm laser irradiation for 5 min, showing no significant impact on bacterial reproduction (Fig. 1j, S7).

Maintaining bacterial viability is crucial for efficient bacterial therapy. First, motile bacteria were capable of transporting IP nanoparticles at a speed of approximately $4.8 \mu\text{m}$ per second within a 0.005 % agarose matrix, functioning similarly to a biological motor (Fig. 2a, b, S8, and Video 1). More notably, the movement of bacteria under NIR with different powers was also explored (Fig. 2c, S9), under proper laser irradiation, the movement speed of the IP@VNP biological motor significantly increased, reaching about $28.4 \mu\text{m}$ per second due to the photothermal effect (Fig. 2c, d, and Video 2). Secondly, the disguise of the IP@VNP@M biological motor within the cell membrane greatly reduced its adsorption and phagocytosis by macrophages, supporting its prolonged circulation in the bloodstream (Fig. 11). Furthermore, the inflammatory targeting effect of the macrophage membrane allowed IP@VNP@M to be preferentially taken up by tumor cells, while normal cells exhibited relatively less uptake (Fig. 2e, S10, and S11). Additionally, the hypoxia-targeting ability of bacteria further enhanced their migration to tumor cells in environments that mimic tumor hypoxia (Figs. 2f, 2h, S12, and S13), even enabling them to cross the fibroblast layer and reach tumor cells under hypoxic conditions (Figs. 2g, 2i, S14, and S15). Importantly, the motility of the photothermal motor, combined with the tumor-targeting capability provided by the cell membrane and hypoxia, allowed IP@VNP@M to penetrate the cell matrix layer and migrated to hypoxic tumors under NIR irradiation. This also enabled deep penetration into the tumor spheroid, where the interior is more hypoxic (Fig. 2j). The biological motor that migrated to tumor cells could be taken up by tumor cells, and also showed the uptake effects of membrane targeting and photothermal enhancement.

Supplementary material related to this article can be found online at [doi:10.1016/j.nantod.2025.102752](https://doi.org/10.1016/j.nantod.2025.102752).

Supplementary material related to this article can be found online at [doi:10.1016/j.nantod.2025.102752](https://doi.org/10.1016/j.nantod.2025.102752).

Thanks to the synergistic effects of VNP and photothermal action, IP@VNP@M internalized by cells could reduce mitochondrial membrane potential of macrophages (Fig. 3a, b) and cause mitochondrial damage, thereby enhancing tumor cell death. Lipopolysaccharides (LPS) on the bacterial surface can induce the polarization of macrophages from the M2 to the M1 phenotype (Fig. 3c). Additionally, photothermal effects promote macrophage polarization, whereas near-infrared (NIR) light alone does not induce such polarization (Figure S16). Notably, the bacteria themselves could induce tumor cell death through the oncolytic effect, and this cell-killin ability was further amplified by the photothermal synergy (Fig. 3c, d, S17). Moreover, the bacteria inherently possessed a certain degree of tumor cell targeting ability, which was further enhanced by membrane encapsulation. Consequently, IP@VNP@M could induce the most significant tumor cell death when exposed to NIR. Conversely, both IP@VNP and IP@VNP@M exhibited negligible cytotoxicity on normal cells and human breast cancer cells in the absence of NIR (Figure S18, S19). These findings suggest that the IP@VNP@M photothermal bio-motor could effectively penetrate the tumor stroma layer, migrate to hypoxic tumors, target tumor cells, and achieve efficient and specific tumor cell killing through the combined effects of photothermal action and bacteria. Additionally, the presence of LPS on the bacterial surface could induce macrophage polarization into the M1 phenotype. Although the ability of IP@VNP coated by the macrophage membrane to induce M1 polarization in macrophages was



(caption on next page)

Fig. 2. Motion behavior analysis of the IP@VNP motor. Typical pathways of a) VNP, b) IP@VNP, and c) IP@VNP subjected to 1.0 W cm^{-2} NIR light exposure for a duration of 180 seconds. d) Statistics of bacterial movement speed. Data are presented as mean \pm SD ($n = 5$). e) Fluorescence microscope images of 4T1 and MCF-10A cells after different treatments. Evaluation of the migration of IP@VNP motor in normal (N) or hypoxic (H) environments. f) Pattern diagram of bacterial migration g) Pattern diagram of bacterial invasion. h) VNP progression towards the lower compartment within environments induced by hypoxia and 4T1 cells. Data are presented as mean \pm SD ($n = 3$). i) VNP penetration into the lower compartment in hypoxia and 4T1 cell-stimulated settings, breaching L929 cellular barriers and reaching the lower chamber. Data are presented as mean \pm SD ($n = 3$). j) LSCM captures of 3D 4T1 multicellular tumor spheroids (MTSs) following diverse treatment regimens. Scanning depth from surface $5 \mu\text{m}$ to $35 \mu\text{m}$. Statistical significance was calculated by one-way ANOVA using the Tukey post-test, giving P values, * $P < 0.05$, ** $P < 0.01$, *** $P < 0.0001$. ns denotes non-significant.

reduced, possibly due to the blockage of LPS exposure and contact with macrophages, IP@VNP@M still induced a significantly higher number of M1 phenotype macrophages compared to the control group, especially under NIR. This effect may be attributed to the release of bacterial LPS triggered by photothermal stimulation, which significantly enhanced the ability to induce M1 polarization in macrophages (Fig. 3e). These findings suggest that IP@VNP@M biological motor not only targets and kills tumor cells but also significantly promotes the polarization of TAM from the M2 phenotype to the M1 phenotype, potentially activating immunosuppressive tumor cells.

To assess the potential of IP@VNP@M for targeted tumor therapy, its *in vivo* distribution was initially examined through *in vivo* fluorescence imaging (Figure S20). The findings revealed that both pure VNP and IP@VNP exhibited a certain degree of tumor accumulation, likely due to their anaerobic orientation. Their enrichment at the tumor site progressively increased over time (Fig. 4a), reaching a peak at 48 h post-injection (Fig. 4b). Notably, when the macrophage membrane was incorporated, the accumulation of IP@VNP@M at the tumor site was significantly enhanced across various time points, with substantial retention observed even at 96 h post-injection (Fig. 4c). Particularly, its liver accumulation was markedly lower compared to the unencapsulated group (Fig. 4d). This phenomenon may be attributed to the macrophage membrane encapsulation, which reduced bacterial phagocytosis by macrophages, thereby extending the systemic circulation time of the bacteria. Additionally, the encapsulation likely minimized the sequestration of naked bacteria by the liver. These factors collectively enhanced the tumor-targeted therapy efficacy of the bacteria while mitigating their toxic side effects (Fig. 4g). Furthermore, photothermal imaging at 24 h post-injection confirmed that the IP-modified bacteria retained the capability for photothermal heating of tumors (Fig. 4e, f). The encapsulation with macrophage membrane further amplified the accumulation of IP@VNP@M at the tumor site, thereby boosting its photothermal tumor heating efficacy.

Further investigation into the tumor treatment efficacy (Figure S21) revealed that the simple VNP group exhibited a certain degree of tumor growth inhibition, and the introduction of IP did not significantly alter the bacteria's therapeutic effect (Fig. 5a). However, after encapsulating the bacteria with the macrophage membrane, the tumor inhibition effect was notably enhanced, attributed to the improved tumor-targeting accumulation. Particularly, with the assistance of NIR light excitation, further targeted accumulation and deeper tumor penetration were achieved via the photothermal-driven IP@VNP@M motor, enabling photothermal synergistic bacterial therapy. This significantly boosted the tumor inhibition effect. By day 15 post-treatment, tumors in the IP@VNP@M+NIR group were nearly eradicated (Figure S22), with the smallest observed tumor volume (Fig. 5b, c) and tumor weight (Fig. 5d). Moreover, the survival time of tumor-bearing mice was substantially extended, from 30 days in the untreated group to 55 days in the photothermal-treated group (Fig. 5e). Throughout the treatment period, the body weight of the mice remained stable, indicating that the administration dose did not cause significant weight changes (Figure S23). This underscores the advanced tumor treatment capability of the IP@VNP@M biological motor.

Further tissue sections and immunofluorescence analysis confirmed that VNP treatment could induce apoptosis of tumor cells and reduce the expression of the tumor proliferation marker Ki67 on day 15 post-treatment (Fig. 5 f, S24). The IP modification on the surface of VNP

did not significantly impact these effects of VNP. However, the encapsulation of VNP with a cell membrane significantly enhanced these therapeutic characteristics, particularly under NIR irradiation, where numerous vacuoles and nuclear-cytoplasmic separation were observed in the tumor tissue (Fig. 5 f). Heat shock protein 70 (HSP70) migrates into the nucleus and binds to denatured chromatin, one of these proteins can translocate to the nucleus under stressful conditions, and a high expression of HSP70 was detected (Fig. 5 f, S24). TUNEL staining results further confirmed significant apoptosis of tumor cells (Fig. 6a, b). These findings reaffirm the highly efficient tumor damage achieved by macrophage membrane-mediated, tumor-targeted photothermal biological motor. Additionally, we discovered that VNP treatment could induce the polarization of TAM towards the M1 phenotype. With membrane-encapsulated targeted delivery, the proportion of M1-polarized macrophages increased. Following synergistic photothermal treatment, driven by the photothermal biological motor effect, macrophages at the tumor site were further polarized to the M1 phenotype (Fig. 6c, d). Given that M1 macrophages are pro-inflammatory and can secrete inflammatory factors to inhibit tumor growth, we further investigated the levels of inflammatory factors in tumor tissues. The results confirmed that VNP alone could indeed promote the secretion of inflammatory factors (TNF- α , IL-1 β and IL-6) (Fig. 6e, S25). Through membrane-mediated and photothermal treatment, IP@VNP@M acts as a photothermal biological motor, further elevating the levels of inflammatory factors at the tumor site, thereby enhancing tumor immunity.

Correspondingly, bacterial motor treatment also elevated the levels of inflammatory cytokines in the blood. However, this increase in inflammatory factors is also a primary indicator of biotoxicity associated with bacterial infection. Notably, during the early stages of bacterial treatment, the significant rise in C-reactive protein (CRP) levels in the blood suggested that bacterial therapy often led to severe acute hematotoxicity, which poses a critical challenge for clinical bacterial treatments. Fortunately, treatment with macrophage membrane-coated photothermal bacterial motor mitigated the initial infection and severe blood inflammation induced by pure VNP bacterial treatment, as evidenced by the reduced expression of TNF- α , IL-1 β , IFN- γ , and CRP (Fig. 6f). Moreover, as the treatment progressed, the biotoxicity induced by this bacterial therapy was gradually alleviated and eventually returned to normal levels. These findings indicate that macrophage membrane-encapsulated photothermal bacteria not only serve as tumor-targeting biological motor for achieving targeted tumor destruction and anti-tumor immune activation but also reduce the risk of infection and blood inflammatory toxicity associated with bacterial therapy.

The liver, a central organ in innate immunity, plays a critical role in defending against microbial invasion, tumor transformation, as well as in liver injury and repair[23]. Motivated by the positive therapeutic outcomes and the observation of prolonged bacterial accumulation in the liver during *in vivo* distribution studies, we further investigated the impact of various treatment groups on liver toxicity. Through evaluating indicators of hepatic functionality such as alanine aminotransferase (ALT), aspartate aminotransferase (AST), along with alkaline phosphatase levels (ALP) (Fig. 7a), our findings revealed that unencapsulated bacteria led to abnormal liver function (Fig. 7b). Additionally, TUNEL fluorescence staining confirmed liver injury (Fig. 7c). Immunohistochemical results showed that apoptosis occurred in over 30 % of liver cells in the VNP group, whereas no signs of damage were observed in the

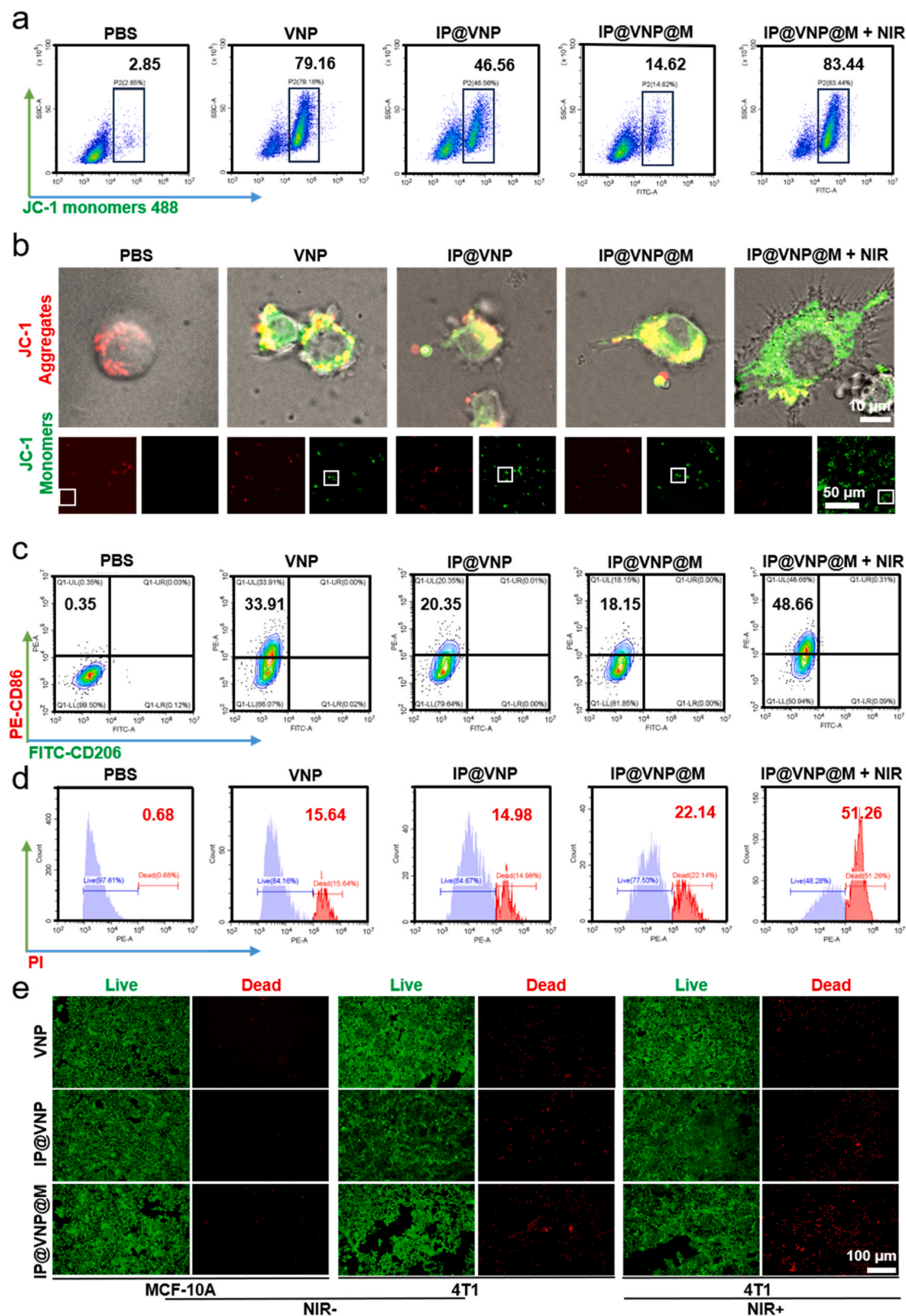


Fig. 3. IP@VNP@M-induced macrophage polarization and tumor deep penetration. a) The measurement of mitochondrial membrane potential was conducted with the JC-1 indicator through flow cytometric examination. The outlined boxes represent the cellular percentage experiencing a drop in mitochondrial membrane potential. b) Representative confocal fluorescence microscopy images of JC-1 aggregate/monomer ratio in M0 macrophage cells treated with different formulations. c) Evaluation of macrophage activation using flow cytometry after exposure to different therapeutic compositions. The scarlet fluorescence signifies cell membranes tagged with PE-CD86 antibody, and the verdant fluorescence denotes cell membranes tagged with FITC-CD206 antibody. d) Flow cytometry analysis for 4T1 live-dead cells. e) MCF-10A cells (without NIR irradiation, NIR-), 4T1 cells (without NIR irradiation, NIR-) and 4T1 cells (with NIR irradiation, NIR+) after adding different formulations in the donor chambers for 24 h. Live: green; Dead: red.

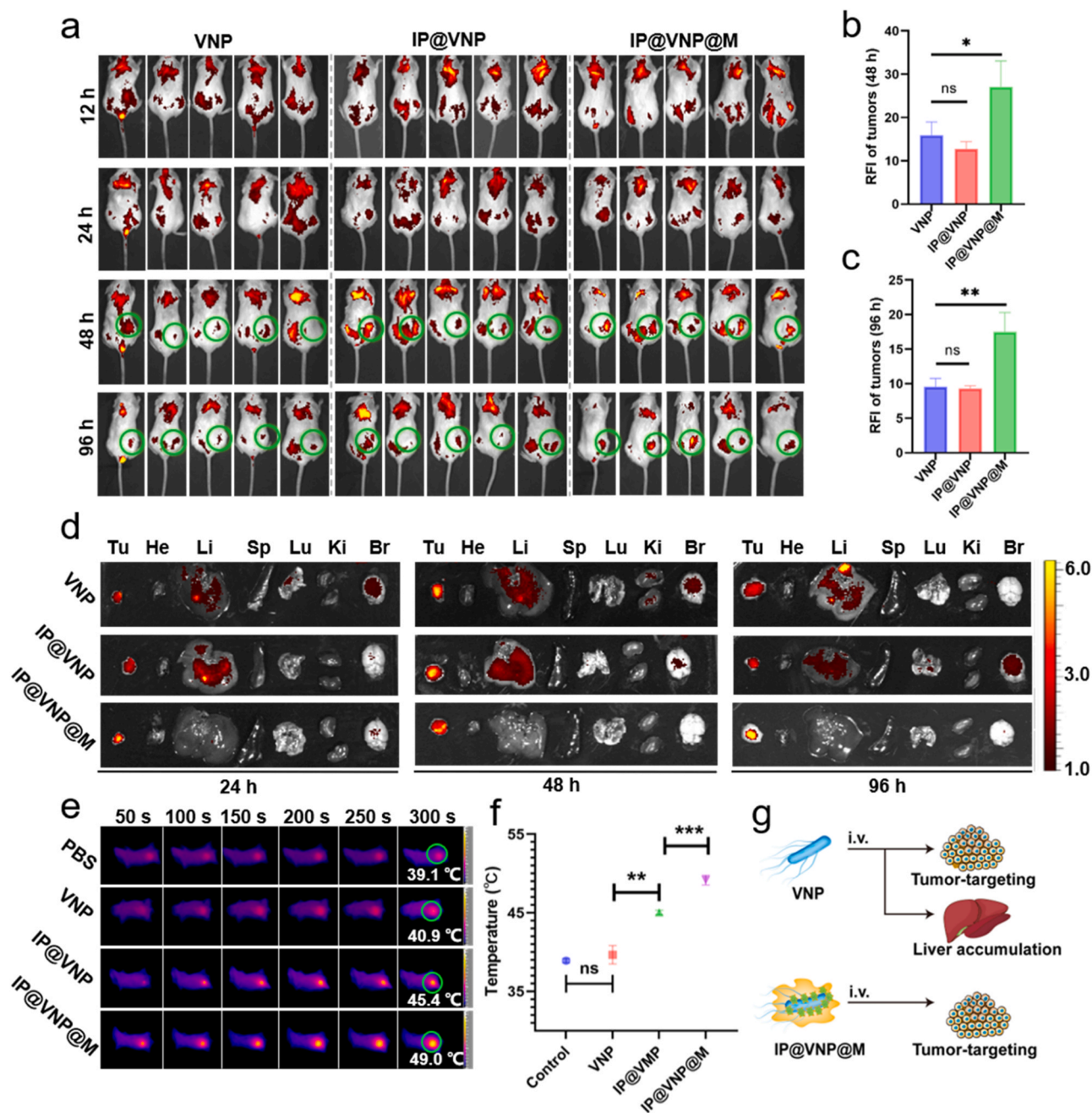


Fig. 4. *In vivo* bioaccumulation of IP@VNP@M in 4T1 tumor-bearing mice. a) Images of 4T1-bearing mice via intravenously injecting different drug formulations. Fluorescence: mCherry. Relative fluorescence intensity (RFI) at the tumor site in the b) 48th and c) 96th hour. d) *Ex vivo* fluorescence images of major organs of 4T1-bearing mice after intravenous injection with different formulations at the dose of $\sim 1 \times 10^5$ CFU for 24 h, 48 h and 96 h, respectively. e) Illustrative thermographic images of tumors in 4T1 mice treated with various formulations under 808 nm laser exposure, along with f) the subsequent thermal variations across different therapeutic cohorts in the breast region. g) Schematic illustrating difference in bacterial distribution before and after coating. Data are presented as mean \pm SD (n = 3). Statistical significance was calculated by one-way ANOVA using the Tukey post-test, giving P values, * $P < 0.05$, ** $P < 0.01$, *** $P < 0.001$. ns denotes non-significant.

liver cells of the IP@VNP@M group (Fig. 7d). Furthermore, H&E staining of liver sections demonstrated nuclear-cytoplasmic separation in the liver cells of the VNP group, while no notable differences were observed between the IP@VNP@M group and the PBS group (Fig. 7e). These findings indicate that unencapsulated bacteria induce significant liver toxicity and potential liver injury.

The antitumor results previously discussed affirm the disguised bacterial system's superior antitumor efficacy *in vivo*. When the drug dosage was increased thirtyfold compared to the dosage used in this study, the 4T1 tumor-bearing mice in both the VNP group and the

IP@VNP group succumbed to acute infection within 12 h, underscoring the greater toxicity and propensity for inflammatory response of unencapsulated bacteria (Figure S26). Furthermore, the biological safety of the VNP dose utilized in this study was assessed. An investigation into the lysis of erythrocytes was carried out to assess the risk of red blood cell destruction after intravenous administration. Results indicated that IP, VNP, nor IP@VNP induced hemolysis, verifying the safety of the intravenous route (Figure S27). Blood analysis and histological evaluations were also performed to ascertain biocompatibility. At the administered dose, all physiological blood parameters in mice treated with

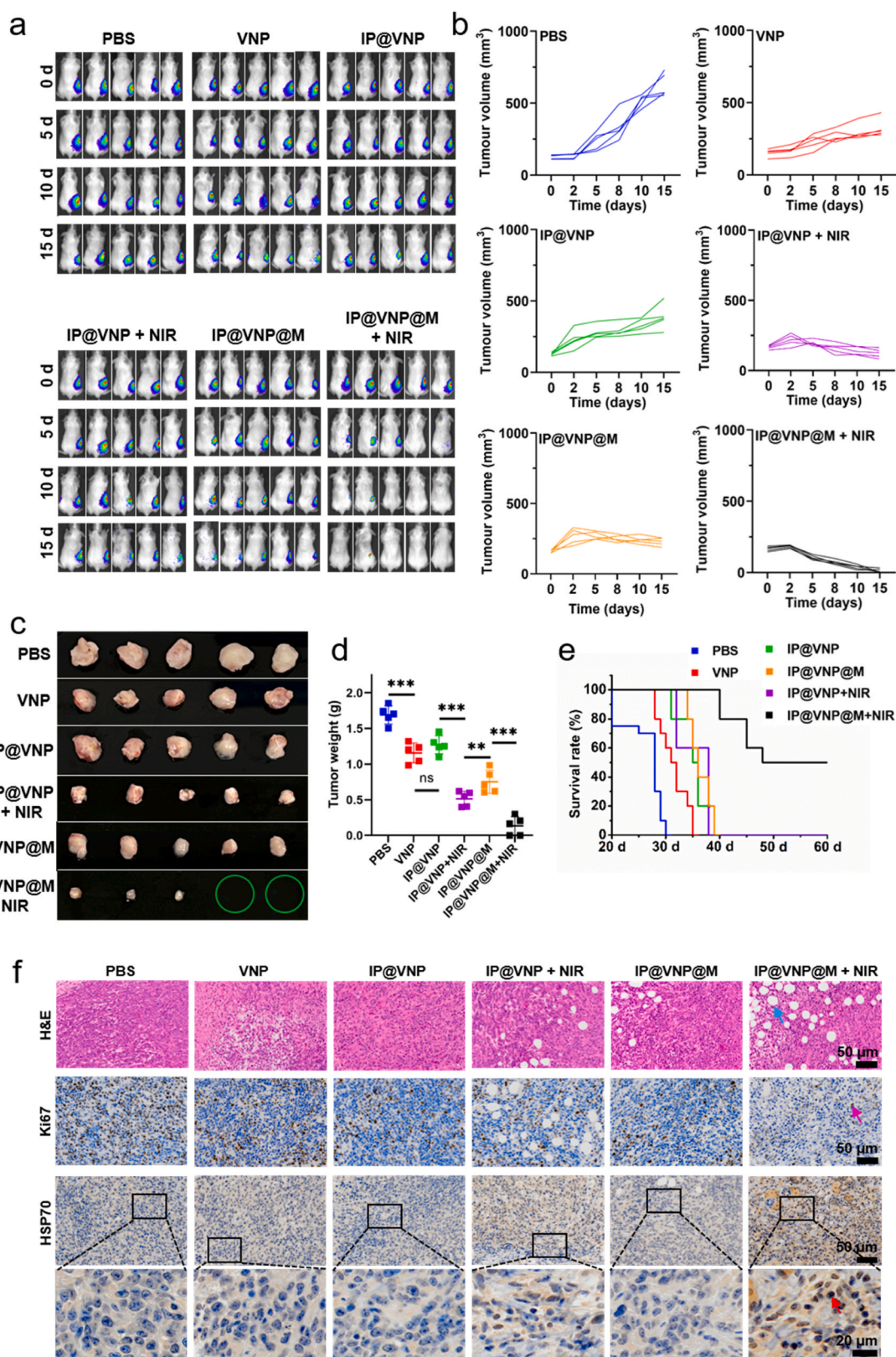


Fig. 5. *In vivo* therapeutic efficacy of IP@VNP@M in mice bearing 4T1-luc tumors. a) Representative *in vivo* bioluminescence images of 4T1-bearing mice after different treatments. b) Tumor growth curves of different treatment groups. c) The images of tumors isolated from tumor-bearing mice 15 d after treatments. d) Quantitative analysis of tumor mass in mice following intravenous injection with diverse preparations (sample size: 5). e) Kaplan-Meier survival curves of different formulations. 4T1 tumor tissues underwent f) H&E, Ki67, and HSP70 staining. The blue arrows indicated the site of fat vacuole. The pink arrows indicated the site of active proliferation. The red arrows represented the HSP-positive cell. Data are presented as mean \pm SD ($n = 3$). Statistical significance was calculated by one-way ANOVA using the Tukey post-test, giving P values, ** $P < 0.01$, *** $P < 0.001$. ns denotes non-significant.

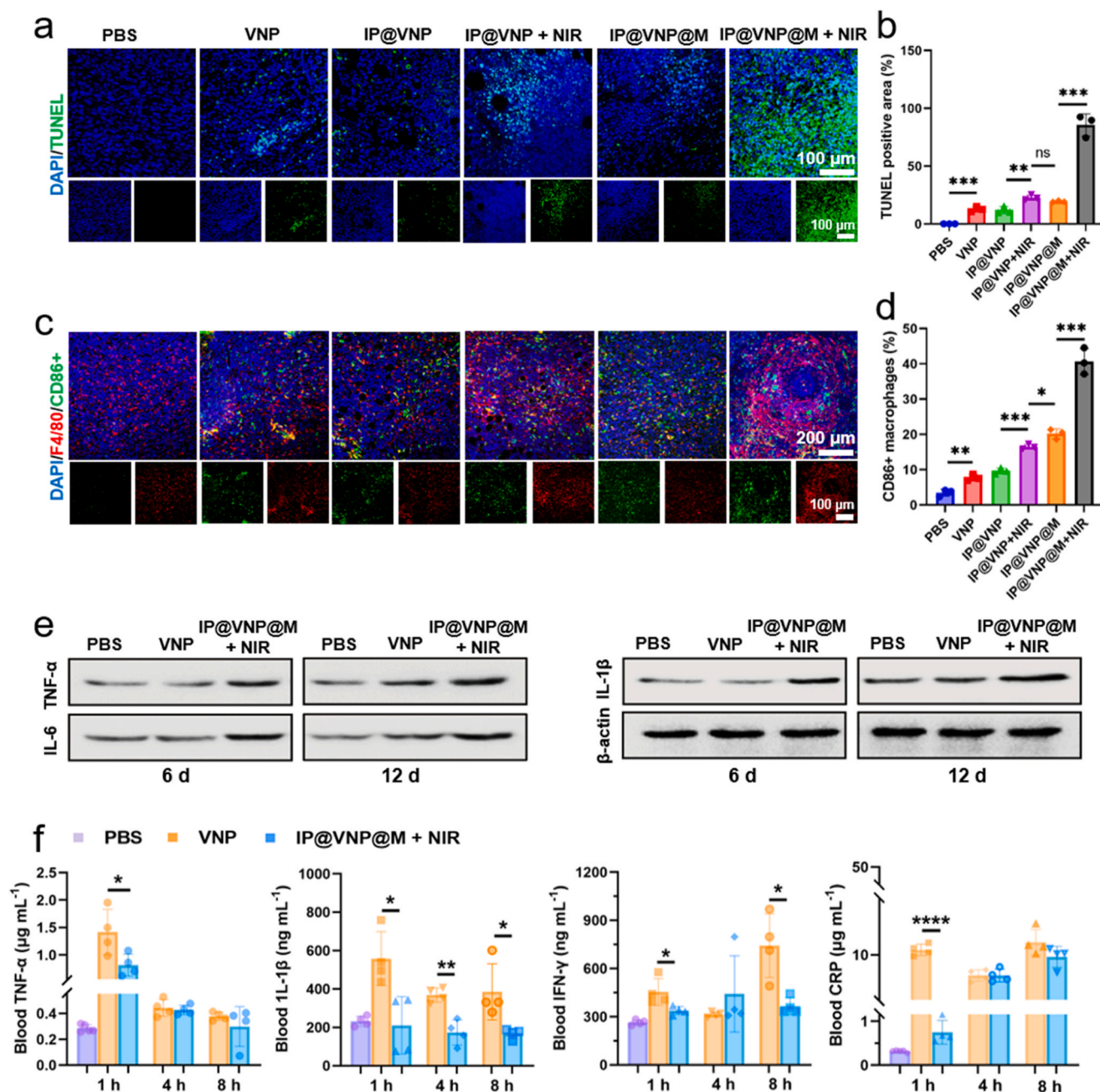


Fig. 6. Assessment of *in vivo* inflammatory responses. a) Assessment of apoptosis in murine tumor tissues via TUNEL labeling post-varied therapeutic interventions. b) Fluorescence quantification of TUNEL positive area. Data are presented as mean \pm SD ($n = 3$). c) Representative tissue immunofluorescence staining of M1 phenotype macrophages (F4/80 CD86+) cells. d) Fluorescence quantification of CD86+ macrophage. Data are presented as mean \pm SD ($n = 3$). e) Expression of integrin TNF- α , IL-6 and IL-1 β in each sample on the 6th and 12nd d after the treatment measured using western blotting. f) Measurement of cytokines including TNF- α , IL-1 β , IFN- γ , and k) CRP in 4T1 tumor-bearing mice. Each mouse received either VNP administration or IP@VNP@M injection (at a dosage of 1×10^5 CFUs) via the caudal vein, with blood samples being collected at specified intervals. Data are presented as mean \pm SD ($n = 4$). Statistical significance was calculated by one-way ANOVA using the Tukey post-test, giving P values, * $P < 0.05$, ** $P < 0.01$, *** $P < 0.001$, **** $P < 0.0001$. ns denotes non-significant.

VNP and IP@VNP@M remained within normal limits, similar to the untreated control group (Figure S28). Histological examinations showed no significant lesions or abnormalities in major organs, attesting to the good biocompatibility and low cytotoxicity of IP@VNP@M (Figure S29). Collectively, the experimental data suggest that the dose used in this study effectively induces tumor necrosis without harming normal tissues.

Conclusion

In this study, we successfully loaded ICG-PLGA photothermal nanoparticles uniformly onto the VNP bacterial surface through covalent linkage and encapsulated the bacteria with M1 macrophage membranes. This process formulated in a macrophage membrane-camouflaged, photothermally-driven bacterial motor (IP@VNP@M). Thanks to the macrophage membrane encapsulation, this IP@VNP@M bacterial motor can evade capture and phagocytosis by blood macrophages, thereby extending its *in vivo* circulation and enabling it to

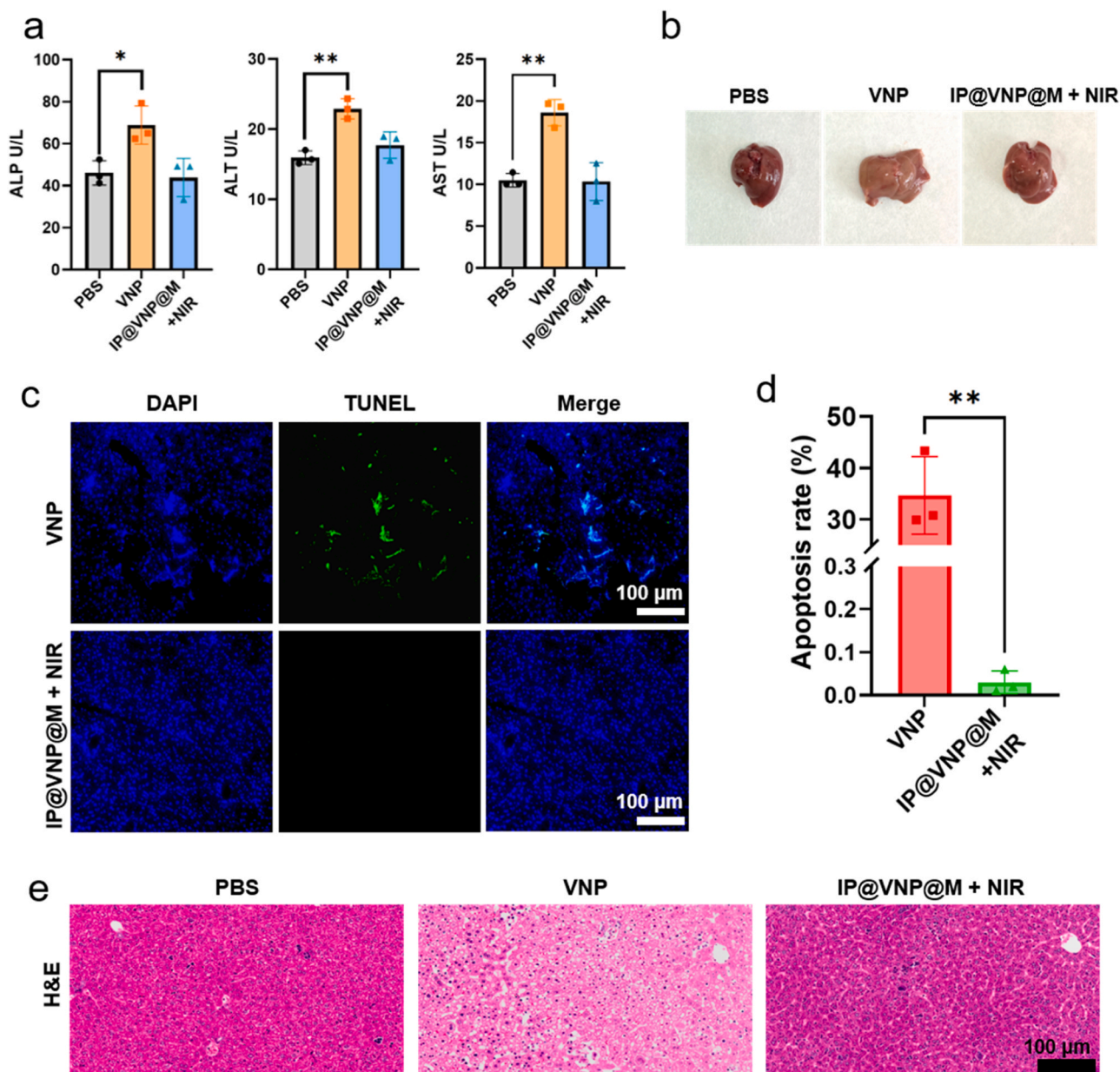


Fig. 7. *In vivo* assessment of hepatotoxicity. a) Measurement of cytokines including ALP, ALT, and AST in 4T1 tumor-bearing mice. Mice harboring 4T1 tumors received intravenous injections of PBS, VNP, or IP@VNP@M (at a dosage of 1×10^5 CFUs) via the caudal vein, with blood samples being collected on the 15th day post-treatment. b) Liver images of mice treated with PBS, VNP or IP@VNP@M (1×10^5 CFUs) through the tail vein. c) TUNEL staining of liver tissues of mice after different treatments. d) Fluorescence quantification of TUNEL positive area. e) H&E staining of mouse liver tissue. Data are presented as mean \pm SD ($n = 3$). Statistical significance was calculated by one-way ANOVA using the Tukey post-test, giving P values, * $P < 0.05$, ** $P < 0.01$.

accumulate in tumors through inflammatory targeting. Crucially, due to the bacteria's hypoxia-tropism and sensitivity to thermal stimulation, this bacterial motor can penetrate deeply into the tumor at four times the original bacterial speed under NIR irradiation and is extensively absorbed by tumor cells. Leveraging the synergy of bacteria and photothermal effects, this bacterial motor can promote the polarization of TAM from the M2 phenotype to the M1 phenotype, facilitating efficient tumor cell death and activating a robust anti-tumor immune response. *In vivo*, this microbial motor therapy significantly prolongs the survival of tumor-bearing mice and reduces the hepatotoxic side effects associated with traditional bacterial therapy. Therefore, this work introduces the concept of "targeted photothermal microbial motor", addressing the challenges of "easy clearance, difficult penetration, and high toxicity" faced by traditional bacterial therapy, and offers a potential new solution for targeted and efficient tumor treatment.

Author Statement

The authors declare that they have no known competing financial interests or personal relationships that could have appeared to influence the work reported in this paper.

CRediT authorship contribution statement

Nie Huifang: Investigation. **Jiang Guangwei:** Investigation. **Zhang Meng:** Writing – original draft, Visualization, Supervision, Software, Methodology, Investigation, Data curation, Conceptualization. **Huang Rongqin:** Conceptualization. **Cyrille Boyer:** Conceptualization. **Dan Peer:** Conceptualization.

Declaration of Competing Interest

The authors declare no competing financial interest.

Acknowledgments

This work was supported by National Natural Science Foundation of China (82172746 and 82473342), International Cooperation Project of Shanghai Science and Technology Innovation Plan (24410741500), and Science and Technology Innovation Plan Laboratory Animal Research Project of Shanghai (23141900400).

Contributions

M.Z., and R.-Q.H. designed the research and wrote the manuscript. M.Z. synthesized and characterized the materials. H.-F.N. involved in the experiments *in vivo*. H.-F.N. and G.-W.J. assisted M.Z. for the data collection and analysis. C. B. and D.P. contributed to the revision and refinement of the manuscript. All authors reviewed and contributed to the final manuscript.

Appendix A. Supporting information

Supplementary data associated with this article can be found in the online version at [doi:10.1016/j.nantod.2025.102752](https://doi.org/10.1016/j.nantod.2025.102752).

Data availability

Data will be made available on request.

References

- [1] N. Pasha, N.C. Turner, Understanding and overcoming tumor heterogeneity in metastatic breast cancer treatment, *Nat. Cancer* 2 (7) (2021) 680–692.
- [2] A. Christofides, L. Strauss, A. Yeo, C. Cao, A. Charest, V.A. Boussiotis, The complex role of tumor-infiltrating macrophages, *Nat. Immunol.* 23 (8) (2022) 1148–1156.
- [3] D.S. Keller, M. Berho, R.O. Perez, S.D. Wexner, M. Chand, The multidisciplinary management of rectal cancer, *Nat. Rev. Gastroenterol. Hepatol.* 17 (7) (2020) 414–429.
- [4] L. Galluzzi, M.J. Aryankalayil, C.N. Coleman, S.C. Formenti, Emerging evidence for adapting radiotherapy to immunotherapy, *Nat. Rev. Clin. Oncol.* 20 (8) (2023) 543–557.
- [5] L. Falzone, R. Bordonaro, M. Libra, SnapShot: cancer chemotherapy, *Cell* 186 (8) (2023) 1816–1816.
- [6] D.J. Irvine, E.L. Dane, Enhancing cancer immunotherapy with nanomedicine, *Nat. Rev. Immunol.* 20 (5) (2020) 321–334.
- [7] S.L. Topalian, J.M. Taube, D.M. Pardoll, Neoadjuvant checkpoint blockade for cancer immunotherapy, *Science* 367 (6477) (2020) eaax0182.
- [8] C.R. Gurbatri, N. Arpaia, T. Danino, Engineering bacteria as interactive cancer therapies, *Science* 378 (6622) (2022) 858–864.
- [9] S. Luca, T. Mihaescu, History of BCG vaccine, *Maedica* 8 (1) (2013) 53–58.
- [10] Q.W. Chen, J.Y. Qiao, X.H. Liu, C. Zhang, X.Z. Zhang, Customized materials-assisted microorganisms in tumor therapeutics, *Chem. Soc. Rev.* 50 (22) (2021) 12576–12615.
- [11] J.X. An, Z.Y. Han, Y.T. Qin, C.X. Li, J.L. He, X.Z. Zhang, Bacteria-based backpacks to enhance adoptive macrophage transfer against solid tumors, *Adv. Mater.* 36 (6) (2024) 2305384.
- [12] K. He, L. Zhang, Y. Ding, Z. Gu, W. Wang, H. Li, Remolding the tumor microenvironment by bacteria augments adoptive T cell therapy in advanced-stage solid tumors, *Signal Transduct. Tar.* 9 (1) (2024) 307.
- [13] N. Zoaby, J. Shainsky-Roitman, S. Badarneh, H. Abumanhal, A. Leshansky, S. Yaron, A. Schroeder, Autonomous bacterial nanoswimmers target cancer, *J. Control. Release* 257 (2017) 68–75.
- [14] X. Ma, X. Liang, Y. Li, Q. Feng, K. Cheng, N. Ma, F. Zhu, X. Guo, Y. Yue, G. Liu, T. Zhang, J. Liang, L. Ren, X. Zhao, G. Nie, Modular-designed engineered bacteria for precision tumor immunotherapy via spatiotemporal manipulation by magnetic field, *Nat. Commun.* 14 (1) (2023) 1606.
- [15] J. Huo, Q. Jia, H. Huang, J. Zhang, P. Li, X. Dong, W. Huang, Emerging photothermal-derived multimodal synergistic therapy in combating bacterial infections, *Chem. Soc. Rev.* 50 (15) (2021) 8762–8789.
- [16] R.S. Li, J. Liu, C. Wen, Y. Shi, J. Ling, Q. Cao, L. Wang, H. Shi, C.Z. Huang, N. Li, Transformable nano-antibiotics for mechanotherapy and immune activation against drug-resistant Gram-negative bacteria, *Sci. Adv.* 9 (34) (2023) eadg9601.
- [17] G.F. Luo, W.H. Chen, X. Zeng, X.Z. Zhang, Cell primitive-based biomimetic functional materials for enhanced cancer therapy, *Chem. Soc. Rev.* 50 (2) (2021) 945–985.
- [18] S.Y. Kwon, H. Thi-Thu Ngo, J. Son, Y. Hong, J.J. Min, Exploiting bacteria for cancer immunotherapy, *Nat. Rev. Clin. Oncol.* 21 (2024) 1–21.
- [19] W. Liu, Y. Liu, H. Li, H. Nie, M. Tian, W. Long, Biomedical micro-/nanomotors: design, imaging, and disease treatment, *Adv. Funct. Mater.* 33 (15) (2023) 2212452.
- [20] C. Pan, D. Xu, Z. Dong, W. Li, D. Kang, W. Chen, Y. Li, M. Zhang, B. Hu, P. Zheng, Effect of temperature decrease on anammox granular sludge: shock and adaptation, *Sci. Total Environ.* 798 (2021) 149242.
- [21] X. Wu, et al., Cell membrane as a promising therapeutic target: from materials design to biomedical applications, *Angew. Chem. Int. Ed.* 136 (2024) e202400249.
- [22] L. Sun, D. Wang, K. Feng, J.A. Zhang, W. Gao, L. Zhang, Cell membrane-coated nanoparticles for targeting carcinogenic bacteria, *Adv. Drug Deliv. Rev.* 209 (2024) 115320.
- [23] C.L. Hsu, B. Schnabl, The gut-liver axis and gut microbiota in health and liver disease, *Nat. Rev. Microbiol.* 21 (11) (2023) 719–733.